JACS
JOURNAL OF THE AMERICAN CHEMICAL SOCIETY

Article

pubs.acs.org/JACS

Impact of Zeolite Aging in Hot Liquid Water on Activity for Acid-Catalyzed Dehydration of Alcohols

Aleksei Vjunov,[†] Miroslaw A. Derewinski,[†] John L. Fulton,[†] Donald M. Camaioni,[†] and Johannes A. Lercher*[,†,‡]

[†]Institute for Integrated Catalysis, Pacific Northwest National Laboratory, P.O. Box 999, Richland, Washington 99352, United States
[‡]Department of Chemistry and Catalysis Research Institute, TU München, Lichtenbergstrasse 4, 85748 Garching, Germany

Supporting Information

ABSTRACT: The location and stability of Brønsted acid sites catalytically active in zeolites during aqueous phase dehydration of alcohols were studied on the example of cyclohexanol. The catalytically active hydronium ions originate from Brønsted acid sites (BAS) of the zeolite that are formed by framework tetrahedral Si atom substitution by Al. Al K-edge extended X-ray absorption fine structure (EXAFS) and ^{27}Al magic angle spinning (MAS) nuclear magnetic resonance (NMR) spectroscopies in combination with density functional theory (DFT) calculations are used to determine the distribution of tetrahedral Al sites (Al T-sites) both qualitatively and quantitatively for both parent and HBEA catalysts aged in water prior to catalytic testing. The aging procedure leads to partial degradation of the zeolite framework evidenced from the decrease of material crystallinity (XRD) as well as sorption capacity (BET). With the exception of one commercial zeolite sample, which had the highest concentration of framework silanol-defects, there is no evidence of Al coordination modification after aging in water. The catalyst weight-normalized dehydration rate correlated best with the sum of strong and weak Brønsted acidic protons both able to generate the hydrated hydronium ions. All hydronium ions were equally active for the acid-catalyzed reactions in water. Zeolite aging in hot water prior to catalysis decreased the weight normalized dehydration reaction rate compared to that of the parent HBEA, which is attributed to the reduced concentration of accessible Brønsted acid sites. Sites are hypothesized to be blocked due to reprecipitation of silica dissolved during framework hydrolysis in the aging procedure.

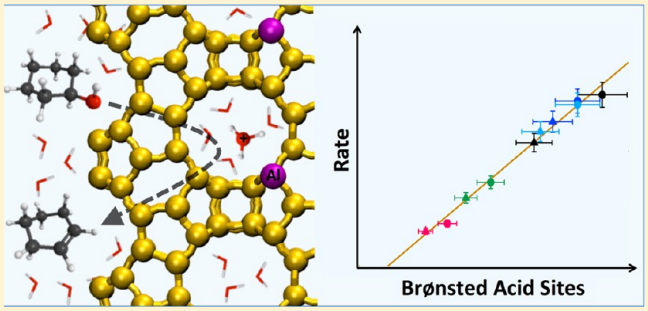

INTRODUCTION

Microporous materials such as zeolites are prospective solid acid catalysts for tailored biomass conversion. The exceptional catalytic performance of these materials is often attributed to the pore environment of the acid sites.[1] The transformation of biomass-derived phenolic molecules (lignin) to diesel range hydrocarbon fuels, for example, requires a complex cascade of chemical reactions, i.e., hydrogenation of phenols to cycloalkanols, dehydration to cyclic olefins, and hydrogenation to cycloalkanes requiring acid catalysis in several steps.[2] Performing these reactions in aqueous media[3] is necessitated in practice by the high water content of the feedstock materials. Achieving practical reaction rates currently requires the reactions be performed at temperatures above 150 °C, conditions under which partial dissolution of zeolites may occur. Previous work suggested that lattice defects, e.g., silanol-nests, are the reactive centers at which the zeolite framework decomposition occurs in hot water,[4] and that the degradation of zeolite HBEA proceeds via selective T−O−T bond hydrolysis.[5] Resasco et al. have shown that curing the Si−OH species via postsynthetic modification of the zeolite with organosilanes allows forming a hydrophobic particle surface[6] that leads to stabilization of the zeolite in aqueous medium. However, an understanding of the effects of hot liquid water on stability of zeolite active sites, the Brønsted acid sites created by Al incorporation in the framework, and the catalyst activity is still critically needed.

To address the above-mentioned questions, we report a systematic study of the impact of zeolite aging in water on the catalytic activity for acid-catalyzed dehydration of alcohols. We have chosen the aqueous dehydration of cyclohexanol as the test reaction, because it is the rate-determining step in phenol hydrodeoxygenation (HDO).[7] A combination of Al extended X-ray absorption fine structure (EXAFS) and magic angle spinning (MAS) nuclear magnetic resonance (NMR) spectroscopies[8] are used to probe the distribution of Al T-sites and to monitor the possible structural changes resulting from the aging of the zeolite in water. Two main points addressed by this work are (1) the effect of hot liquid water on the active site integrity and catalytic reaction TOF normalized to the number of Brønsted acid sites (BAS), and (2) the influence of Al-concentration in the zeolite framework on the TOF in aqueous

Received: June 13, 2015
Published: August 3, 2015

DOI: 10.1021/jacs.5b06169
J. Am. Chem. Soc. 2015, 137, 10374−10382

Table 1. Studied HBEA Zeolite Samples with Corresponding Elemental Analysis, BET ,and Pyridine Adsorption Characterization Data

catalyst[a]	Si/Al ratio[b]	Al concentration (μmol/g)[b]	mesopore volume (cm^3/g)	micropore volume (cm^3/g)	total Brønsted acid site concentration (μmol/g)[c]	strong Brønsted acid site concentration (μmol/g)[c]
HBEA30	15	890	0.27	0.15	400	330
HBEA37	19	740	0.18	0.18	360	260
HBEA52	26	540	0.09	0.20	360	280
HBEA80	40	360	0.07	0.24	220	210
HBEA150	75	190	0.15	0.18	150	140
HBEA30w	15	910	0.16	0.10	290	230
HBEA37w	18	780	0.12	0.10	320	290
HBEA52w	24	570	0.07	0.09	300	250
HBEA80w	41	360	0.11	0.12	180	170
HBEA150w	66	220	0.15	0.08	115	110

[a]Zeolite samples that were aged in water prior to catalytic testing are labeled with "w". [b]Determined from elemental analysis. [c]Determined from pyridine adsorption.

phase. In this work, we demonstrate that all accessible Brønsted acid sites irrespective of their concentration in the zeolite framework are equally active for acid-catalyzed dehydration of cyclohexanol in water. Our results indicate that further research is needed in the field of zeolite postsynthetic modification leading to materials with very few defects and highly accessible BAS as well as provide a conceptual pathway for the successful use of zeolites in water.

RESULTS AND DISCUSSION

Catalyst Properties. In this work we used four lab-synthesized (HBEA30, HBEA37, HBEA52, HBEA80) catalysts and one commercial (HBEA150) catalyst. The properties of these catalysts, as analyzed by elemental, Brunauer–Emmett–Teller (BET)[9] and temperature programed desorption of bases, are compiled in Table 1. The 48 h 160 °C water treated samples are also listed in Table 1 and are marked with a suffix "w".

To determine the surface morphologies and particle size distributions of the studied catalyst, we have imaged all samples by He ion microscopy (HIM). Let us first turn to the parent HBEA catalysts, which all have similar morphologies (panels a and b in Figures 1–5). The particle sizes for these zeolites vary from ~220 to 450 nm, increasing in size with the Si/Al ratio. Note that the particles are agglomerates of small crystals, which leads to the formation of intercrystal mesopores. The HIM images obtained for the water treated samples (Figures 1–5, panels c and d) do not show substantial changes in particle sizes; however, particle surfaces appear smoothened compared to the parent samples. We attribute this to the removal and reprecipitation of silica, both dissolved from the framework and amorphous synthesis remnants.

Table 1 also reports the micro- and mesoporosity of the zeolites determined by the BET analysis of N_2 adsorption. The parent samples have pore volumes ranging from about 0.30 (HBEA52 and HBEA80) to 0.42 (HBEA30) $cm^3\ g^{-1}$. In general, the microporosity varies inversely with the concentration of Al. In the case of the lab-synthesized zeolites, the micropore volume increases with decreasing Al concentration. An opposite trend is observed for the mesopore volumes originating from the inter crystal voids in the agglomerates of small crystals. This is particularly evident in the samples with high Al content (HBEA30 and HBEA37). This tendency to smaller crystallites leads to higher concentrations of silanols terminating the crystals and in consequence to a higher

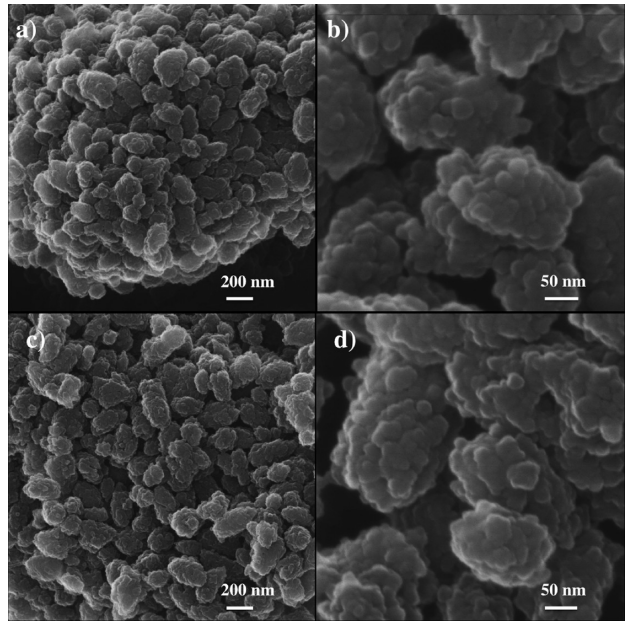

Figure 1. HIM images of the untreated (a and b) and the 48 h 160 °C (c and d) water treated HBEA30 samples. The magnification is reported in the plots.

concentration of mesopores.[10] The commercial HBEA150 zeolite, which has the lowest Al concentration (Si/Al = 75), exhibits micro- and mesoporosity comparable to those observed for the lab-synthesized HBEA30 and HBEA37 with Si/Al ratios of 15 and 19, respectively. We hypothesize that the porosity of the commercial HBEA150 sample indicates that it had undergone postsynthetic modification. Typically, commercial zeolites[11] are synthesized with low Si/Al ratios and are then modified via a sequence of steaming and/or mineral acid leaching steps.[10] The removal of Al from the zeolite framework leads to additional mesoporosity[12] as well as to an increased concentration of Si–OH defect sites, which greatly influence the hydrothermal stability of such zeolites.[5]

In the case of the HBEA samples aged in water prior to catalytic testing, the zeolite pore volumes have decreased by ~30–40% compared to the parent material (Table 1) for all catalysts. This pore volume decrease is due to the destruction of both micro- and mesopores (Table 1). We attribute the observed changes to hydrolysis of framework Si–O–Si groups

DOI: 10.1021/jacs.5b06169
J. Am. Chem. Soc. 2015, 137, 10374–10382

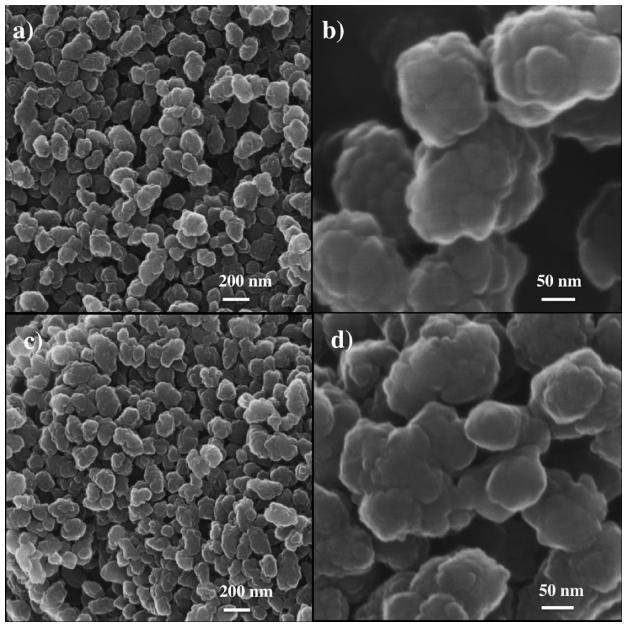

Figure 2. HIM images of the untreated (a and b) and the 48 h 160 °C (c and d) water treated HBEA37 samples. The magnification is reported in the plots.

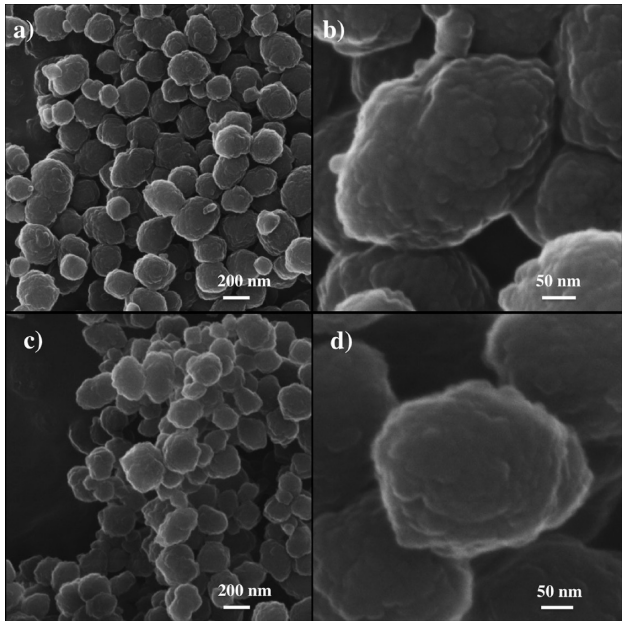

Figure 3. HIM images of the untreated (a and b) and the 48 h 160 °C (c and d) water treated HBEA52 samples. The magnification is reported in the plots.

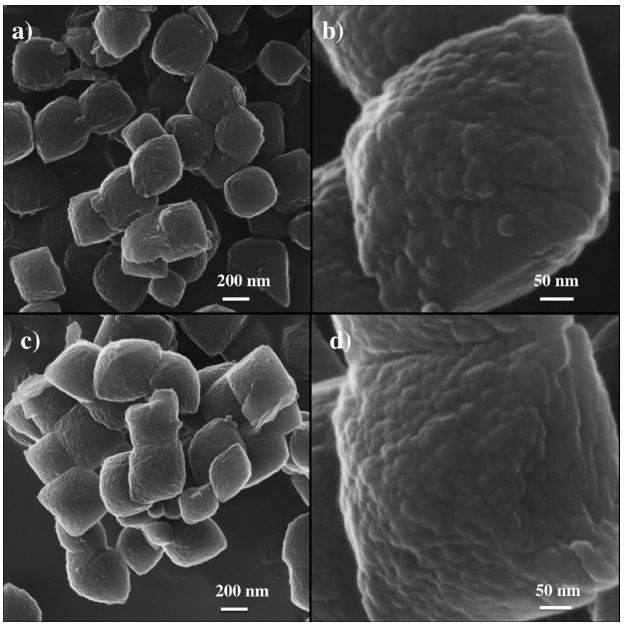

Figure 4. HIM images of the untreated (a and b) and the 48 h 160 °C (c and d) water treated HBEA80 samples. The magnification is reported in the plots.

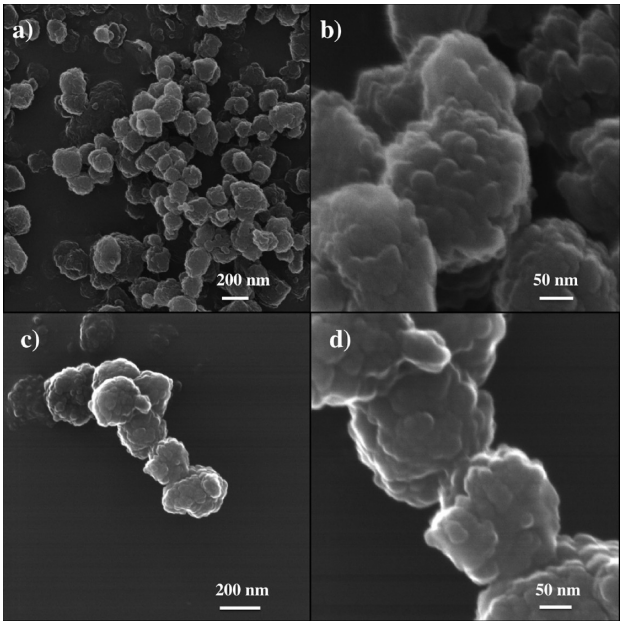

Figure 5. HIM images of the untreated (a and b) and the 48 h 160 °C (c and d) water treated HBEA150 samples. The magnification is reported in the plots.

and Si−O−Si−OH groups at the surfaces of crystallites in the agglomerate particles.

Table 1 also compiles the concentrations of strong and total Brønsted acid sites determined from the IR-spectra of adsorbed pyridine. The concentrations of BAS are in all cases lower than the concentrations of Al and the difference increases with the Al concentration. HBEA52 has a BAS concentration similar to HBEA37, even though HBEA37 has 37% more Al than HBEA52. We suggest the discrepancy between Al and BAS is largely due to a fraction of the BAS being inaccessible to sorbates. Compared to the parent zeolites, the water treated zeolites showed an approximately 15−30% decrease in both the total and strong BAS concentration. We suggest this decrease is due to pore blocking via dissolution and reprecipitation of silica causing more Al T-sites to become inaccessible to pyridine molecules.

X-ray Diffraction. The XRD patterns for the parent and water treated samples are shown in the Supporting Information (SI) and are used to estimate the degree of crystallinity of the HBEA[13] samples. The XRD signal intensity at $2\theta = 7.7°$ varied without a clear trend for the parent samples. For the water treated samples, the XRD intensity of this peak was reduced to

DOI: 10.1021/jacs.5b06169
J. Am. Chem. Soc. 2015, 137, 10374−10382

~25−40% of that observed for the respective parent material. In contrast, the intensity of the reflection for HBEA37w was little changed by water.

Al XAFS Analysis. The variation of the X-ray absorption ($x\mu E$) in the energy region of the Al XANES is shown in Figure 6a. The strong signal intensity observed at 1566 eV for all

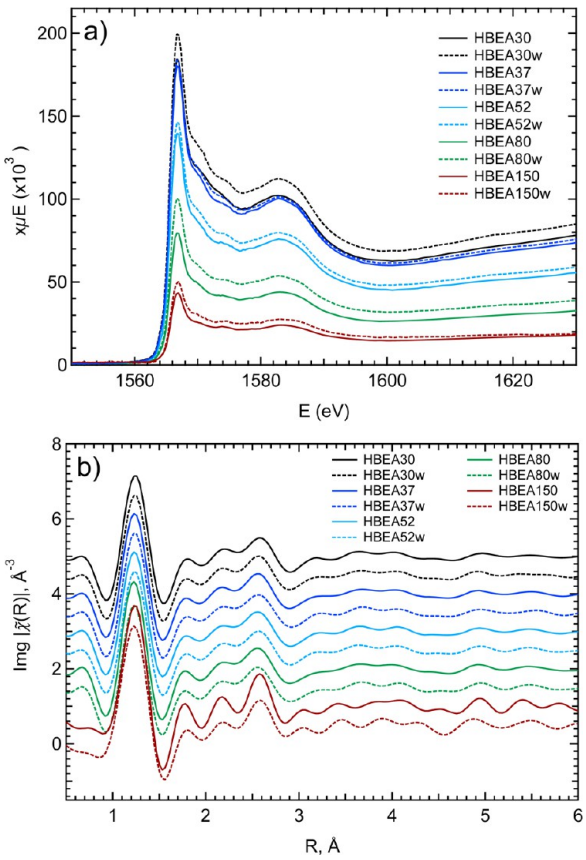

Figure 6. (a) XANES $x\mu E$ spectra for the parent and water treated HBEA samples. Note the increase in Al intensity for the water treated samples suggesting higher Al concentration in these samples. The observation is attributed to selective Si-removal in water. (b) EXAFS Img[$\bar{\chi}(R)$] spectra for the parent and water treated HBEA samples. The spectra are offset (y-axis) for better visualization. The color-coding is reported in the legend.

samples is assigned[14] to the tetrahedral Al in the zeolite samples. The prominent tetrahedral Al feature is attributed primarily to excitations from Al 1s to a mixture of O 3p and Al 3p states.[8] In the case of lab-synthesized HBEA, both parent and water-treated, there is no indication of 5- or 6-coordinated Al species, which are typically observed at 1567.5 and 1568 eV, respectively.[15] In the case of the commercial HBEA150 and HBEA150w, the XANES suggest 7 and 8% octahedral Al^{3+}, respectively. The Al signal intensity is slightly enhanced for all water treated samples, suggesting that the overall Al concentration in the zeolites was slightly increased after the water treatment due to Si dissolution from the zeolite framework. This observation is in agreement with the changes in the HBEA Si/Al ratios determined from element analysis (Table 1).

The EXAFS Img[$\bar{\chi}(R)$] spectra for the parent and water treated HBEA samples are shown in Figure 6b. With the exception of HBEA150, the Img[$\bar{\chi}(R)$] of the parent HBEA samples appear quite similar in representation. This observation suggests that in the case of HBEA30, HBEA37, HBEA52, and HBEA80 Al is distributed similarly among the same sets of T-sites. Since the EXAFS spectra indicate that the Al−O bond and Al−Si atom distances of the 48 h 160 °C water treated samples are nearly identical to those of the parent samples, the treatment is suggested not to lead to selective Al removal from the framework. We note that peak positions and intensity in the region from 2−5 Å in the EXAFS spectra of HBEA150 and HBEA150w differ only in minor aspects from those observed for the lab-synthesized samples.

Quantitative Analysis from ^{27}Al NMR. The NMR spectra of the parent and water treated samples are shown in Figure 7a,b. The NMR chemical shifts calculated[8] for the 9 different T-

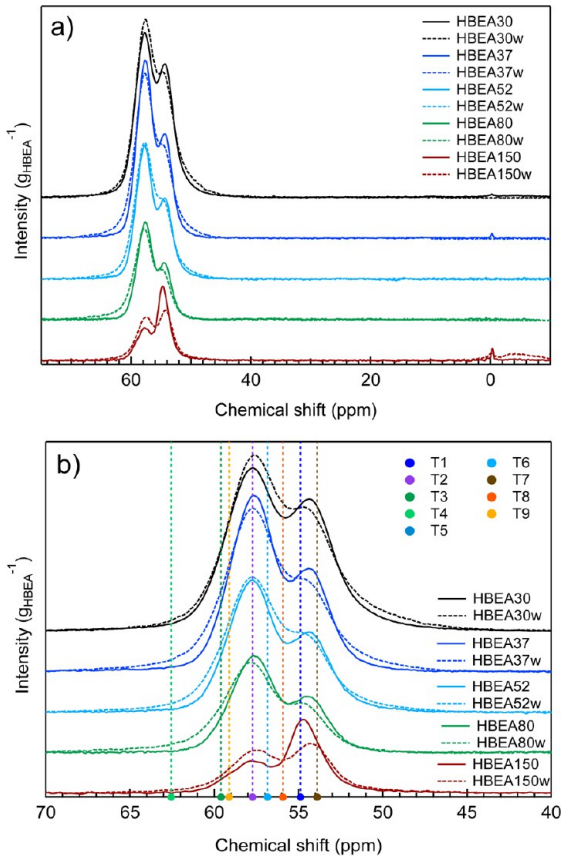

Figure 7. ^{27}Al MAS NMR spectra of the parent and 48 h 160 °C water treated HBEA samples are shown in (a). The region for the tetrahedral Al signal is shown in (b). The chemical shift values for the nine T-sites of HBEA calculated using DFT are shown for reference. The color-coding is reported in the legend.

sites of HBEA are also shown for reference. The measured chemical shifts are in agreement with chemical shift values reported for HBEA previously.[16,17]

While the lab-synthesized samples exhibit almost no Al in octahedral coordination (0 ppm region[18]), a small fraction of octahedral Al species was observed for the commercial (HBEA150 and HBEA150w) samples. The NMR region assigned to the 4-coordinated framework Al of the HBEA spans from 52−62 ppm and has two distinct peaks at 54 and 57 ppm. There is no indication of 5-coordinated and extra-framework tetrahedral Al, which are typically observed in NMR in the regions of ~30−40[19,20] and ~40−45 ppm,[21] respectively. The HBEA30, HBEA37, HBEA52, and HBEA80, as well as the

DOI: 10.1021/jacs.5b06169
J. Am. Chem. Soc. 2015, 137, 10374−10382

respective water treated samples, show a similar NMR peak shape and intensity. The main tetrahedral Al peak accounting for 3/5 of the spectral intensity was observed at 57.6 ppm, the shoulder accounting for ~2/5 at 54.3 ppm. A significant change was observed for the HBEA150 and HBEA150w samples. The water treatment resulted not only in a downfield shift of the tetrahedral Al NMR peak, but also in a change of the peak intensity. Specifically, both tetrahedral Al NMR peaks of HBEA150 are shifted by −0.3 ppm and a fraction of tetrahedral Al observed at 54.7 ppm (HBEA150) is hypothesized to be selectively converted to octahedral Al.

Overall, the NMR spectral intensities are consistent with the Al concentrations measured by elemental analysis (Table 1). The water treatment resulted in two changes in the NMR spectra: (1) a minor downfield shift in peak positions and (2) a slight broadening of the peaks, which is attributed to distortions in the Si-structure induced by hydrolysis of Si−O−Si linkages in the vicinity of the Al T-sites. Both changes lead to inhomogeneously broadened NMR peak shapes consisting of a continuum of independent lines,[22] due to the introduction of defects into the symmetric structure of the HBEA framework. The broadening also affects the quadrupolar coupling and, therefore, the chemical shift.

Al-Distribution in HBEA. The distribution of Al in HBEA was determined from the combination of EXAFS and NMR supported by theory as described in the Experimental Section and prior work.[5,8] For the EXAFS analysis, the nine T-sites of HBEA are grouped into three sets, A (T1, T2, T5, T6), Set B (T3, T4), and Set C (T7, T8, T9), based on the similarities of the EXAFS spectra of the T-sites of HBEA predicted from DFT calculated structures. Molecular Dynamics (MD) EXAFS spectra are calculated for one representative Al T-site of each set. Linear combinations of these MD-EXAFS calculated spectra along with the EXAFS spectrum of $Al(H_2O)_6^{3+}$, as a model of the octahedral Al sites, were then used to fit the measured EXAFS spectra. The measured NMR spectra are fitted using chemical shift values for the nine T-sites of HBEA calculated for an $Al-(OSi)_4(OH)_{12}^-$ cluster derived from the DFT optimized HBEA unit cell.[5,8] The Al distributions determined for the parent and water treated HBEA samples are summarized in Table 2S.

The Al EXAFS results indicate that the Al preferentially populates T-sites of Set A (T1, T2, T5, T6) in the parent zeolite samples. Because the fit quality did not improve significantly when we included contributions of either Set B or Set C sites,[8] an accurate determination of the Al fraction populating set B and/or C from the EXAFS analysis alone remains ambiguous. However, the tetrahedral Al contributions can be further resolved by fitting the NMR spectra using the chemical shift values calculated from DFT. The measured NMR spectra are fitted such that the peak intensities, the offset relative to the aqueous Al^{3+} reference, the peak width and peak shape were optimized with constraints that the peaks have the same widths, Guassian-Lorentzian ratios and absolute chemical shifts of the Al T-sites.[5,8] When different values for the aqueous Al^{3+} reference were allowed, several unique fits were obtained for each of the samples. The best fit was selected as the one that is in agreement with the distribution determined from EXAFS analysis, which indicated ~75% of Al T atoms occupied Set A sites. The analysis of the NMR spectra then shows that this Al is distributed in sites, T1 and T2. The remaining ~25% Al is distributed in sites T7 and T9. In the synthesized HBEA samples, 55% of framework Al populates the T2 sites. Al also populates the T1 and T7 sites, each to a level of ~15−25%. The T9 sites are populated to a level of up to 14%. On the contrary, in the case of the commercial HBEA150 zeolite, approximately half of the tetrahedral Al populates the T1 site. The T2 site is populated at ~20%. The remaining tetrahedral Al is distributed statistically between sites T7 and T9. The NMR spectral fitting results indicate that Al does not populate to a significant extent the T3, T4, T5, T6, and T8 sites in any of the samples. Finally, the fraction of Al in T-sites T1 and T2 increases with the increase in the Si/Al ratio at the expense of sites T7 and T9.

In the case of the water treated samples, HBEA30w, HBEA37w, HBEA52w, and HBEA80w, significant changes in the Al distribution compared to the respective parent samples were not observed. The analysis shows that the water treatment causes neither selective Al removal nor substantial redistribution of Al among the zeolite T-sites. The Al-distributions determined for both the parent and water treated samples by EXAFS and NMR are in very good quantitative agreement and suggest a high concentration of Al in T2 sites in the lab-synthesized samples.

In the case of HBEA150 a fraction of tetrahedral Al was concluded to be converted to octahedral coordination. We speculate that the more prominent transformation (compared to the lab-synthesized samples) is due to a higher concentration of framework defects.

We suggest that the population of T-sites is due to the kinetic control during zeolite synthesis, tentatively attributed to the directing role of tetraethylammonium hydroxide (TEAOH) used as template for the lab-synthesized HBEA. Previously, the key role of the template was shown for ferrierite, indicating that the organic template preferentially occupied well-defined positions within the void volume of the zeolite framework.[23] The synthesis conditions used in this work have resulted in the formation of isolated (determined from ^{29}Si NMR) Al T-sites. This finding simplifies the analysis by eliminating to consider effects of Al-pairing. Dedecek et al. have shown that the sources of Si and Al, as well as synthesis temperature, can affect Al distribution and alter the pattern of the $Al-O-(Si-O)_n-Al$ sequences.[24]

^{29}Si MAS NMR. The acquired single pulse (SP) and cross-polarization (CP) ^{29}Si NMR spectra for the parent and water treated HBEA zeolites are shown in Figures 8 and 9,

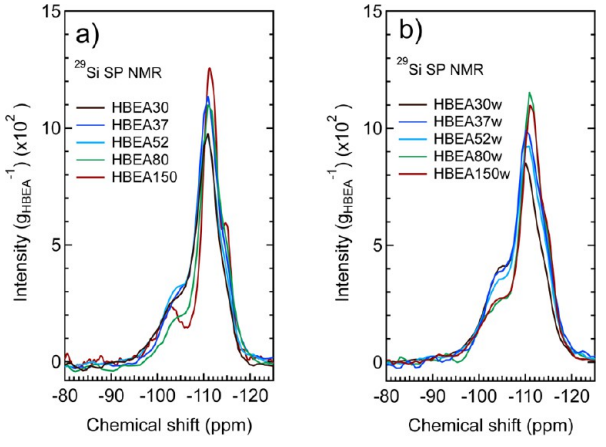

Figure 8. ^{29}Si MAS NMR single pulse (SP) spectra of the parent (a) and water treated (b) HBEA samples. The color-coding is shown in the legend.

DOI: 10.1021/jacs.5b06169
J. Am. Chem. Soc. 2015, 137, 10374−10382

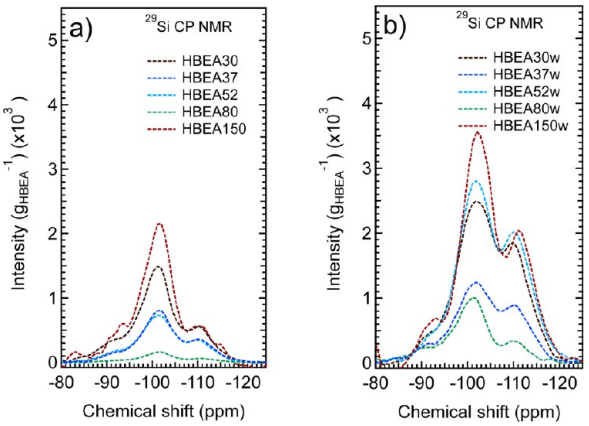

Figure 9. ^{29}Si MAS NMR cross-polarization (CP) spectra of the parent (a) and water treated (b) HBEA samples. The color-coding is shown in the legend.

respectively. The SP NMR spectra for the parent and water treated HBEA samples are shown in Figure 8, panels a and b, respectively. In the SP NMR, the main peak centered at approximately −111.5 ppm is attributed to the Si Q^4 atoms.[25] Shoulder peaks left and right of the main peak are due to the distribution of NMR chemical shifts of the nine T-sites of HBEA. The signal at approximately −103 ppm[26] is assigned to the Si Q^3 [Si(OSi)$_3$OAl]. The variation of intensity for this peak is explained by the differences in the Si/Al ratios of the studied samples. The SP NMR spectra show little intensity at −98 ppm, indicating that the fractions of Si in Q^2 sites[27] as well as in paired Al sites (Al−O−Si−O−Al) are negligible. The SP NMR spectra of the treated samples reflect the changes in the Si−O backbone of the zeolites in water. A slight decrease in signal intensity, as well as broadening of the NMR spectra, is observed for all samples and is attributed to an increase in structural defects, as the zeolite framework is hydrolytically degraded.

The CP NMR spectra for the parent and water treated HBEA samples are shown in Figure 9, panels a and b, respectively. The large peak at approximately −101 ppm is assigned to the Si(OH)(OSi)$_3$ species.[28] The Si Q^3, Si(OSi)$_3$OAl, atoms that neighbor Al T-sites are assigned to NMR signals around −106 ppm.[26] The CP NMR signals from −110 to −115 ppm are assigned to the Si Q^4 atom of the zeolite.[26] In the case of the HBEA30, HBEA37, HBEA52 and HBEA80 zeolites, the CP NMR spectra of the parent samples exhibit a general trend of an increase of signal intensity in the Si Q^3 region with decreasing Si/Al ratios in the sample. The higher Al concentration in the synthesized HBEA leads to the formation of smaller crystallites (kinetic control during synthesis), which in turn leads to a high concentration of intercrystal growth faults. These faulting regions contain a high concentration of Si−OH defect sites and Si−OH nests. The signal intensity at −101 ppm (Si Q^3 region) is markedly increased for the water treated samples, suggesting an increased concentration of Si−OH groups within the lattice structure (Si−OH nests).[29]

While the CP NMR signal is enhanced for all water treated samples, there is no correlation with the Al concentration in the sample. On the basis of this observation, we hypothesize that the concentration of Si−OH defects, not the Al concentration, determines the integrity of the HBEA framework. Note that the CP NMR intensity of the water treated samples is in qualitative agreement with the changes observed in the XRD patterns: as the intensity of the reflection at 2θ = 7.7° decreases, the concentration of Si−OH (CP NMR) increases. For example for the lab-synthesized samples, both XRD and CP NMR signal intensities are comparable between HBEA37w and HBEA80w as well as between HBEA30 and HBEA52w. Interestingly, the degree of crystallinity (based on the peak at 2θ = 7.7°) is lower for the parent HBEA30 and HBEA52. It appears that while the rates of hydrolysis are similar for these HBEA zeolites, the samples with lower concentrations of lattice defects exhibit greater stabilities in water.

The formation of surface OH groups (typically a signal at −100 ppm)[30] cannot be unambiguously determined from the CP NMR due to substantial peak broadening. Lippmaa et al. showed that the higher chemical shift value can be related to a rearrangement in the neighboring Si−OH groups in geminal [Si(OH)$_2$(OSi)$_2$] or vicinal [(OSi)$_3$Si−OH HO−Si(OSi)$_3$] conformation.[31] As only a minor signal (by comparison) is observed at −90 ppm,[32,33] which is attributed to the Si Q^2 [Si(OH)$_2$(OSi)$_2$], most Si−OH groups are suggested to be in a vicinal conformation in both the parent and water treated samples.

Catalytic Testing. The activities of the parent and water-aged HBEA zeolites were assessed on the aqueous phase cyclohexanol dehydration reaction. Cyclohexene was observed

Table 2. Catalytic Performance of the Parent and Water Zeolite Samples Is Tested on the Cyclohexanol Dehydration Reaction[a]

catalyst	Si/Al ratio[b]	cyclohexene yield (%)[c]	rate of cyclohexene formation (μmol$_{cyclohexene}$ × g_{HBEA}^{-1} × s^{-1})	TOF normalized to strong BAS[d] concentration (mol × $mol_{Strong\ BAS}^{-1}$ × s^{-1}) × 10^3	TOF normalized to total BAS [c] concentration (mol × $mol_{Total\ BAS}^{-1}$ × s^{-1}) × 10^3
HBEA30	15	11.4	14.6 ± 1.0	45 ± 3	36 ± 3
HBEA37	19	11.1	14.1 ± 1.0	54 ± 4	39 ± 3
HBEA52	26	11.0	13.8 ± 1.0	50 ± 4	38 ± 3
HBEA80	40	6.0	7.5 ± 0.5	35 ± 3	34 ± 2
HBEA150	75	3.2	4.1 ± 0.3	28 ± 2	28 ± 2
HBEA30w	15	8.5	10.7 ± 0.8	47 ± 3	37 ± 3
HBEA37w	18	9.9	12.4 ± 0.9	43 ± 3	39 ± 3
HBEA52w	24	9.2	11.6 ± 0.8	47 ± 3	39 ± 3
HBEA80w	41	4.9	6.2 ± 0.4	36 ± 3	34 ± 2
HBEA150w	66	2.8	3.5 ± 0.3	30 ± 2	30 ± 2

[a]The rates of formation as well as TOF are reported for cyclohexene, the main dehydration product. Reaction conditions: 80 mL 0.33 M cyclohexanol + 58 mg HBEA reacting at 160 °C. [b]Determined from elemental analysis. [c]Determined yield for the 1 h reaction. [d]BAS concentration accuracy estimated at ±10%

DOI: 10.1021/jacs.5b06169
J. Am. Chem. Soc. 2015, 137, 10374−10382

to be the primary product in this reaction (see Table 2 for details). Dicyclohexyl ether was also formed in the initial reaction phase with a maximum yield well below 1%, and is hence not discussed further. Table 2 also reports two turnover frequencies, one normalized only to the concentration of strong BAS (mol $mol_{Strong\ BAS}^{-1}$ s^{-1}), and the other normalized to the concentration of all (weak and strong) BAS ($mol_{cyclohexene}$ $mol_{Total\ BAS}^{-1}$ s^{-1}). In the first case, the TOF based on strong BAS, we note that the TOF varies by nearly a factor of 2. In the second case, the TOF based on the total BAS ranges over values that differ only by a factor of 1.4.

The initial rates ($mol_{cyclohexene}$ g_{HBEA}^{-1} s^{-1}) of cyclohexene formation catalyzed by the water treated samples are typically ~25% lower than the rates catalyzed by the corresponding parent samples. However, as we have observed (Table 1) that the water treatment reduces the BAS concentrations by ~25%, the TOF for treated and parent catalysts are considered to be identical.

Figure 10 shows the rate of cyclohexene formation plotted against the concentrations of (a) total and (b) strong BAS. It is seen that the rates are linearly correlated with the total BAS giving an R^2 = 0.989 compared to R^2 = 0.920 for the strong BAS. Note that in either case some BAS determined by pyridine adsorption are not active in the dehydration of cyclohexanol. This could be due to the inherent differences for the accessibility of pyridine and cyclohexanol to the hydronium ions, or it could be that a constant fraction of sites is destroyed or converted by the immersion in hot water during catalysis.

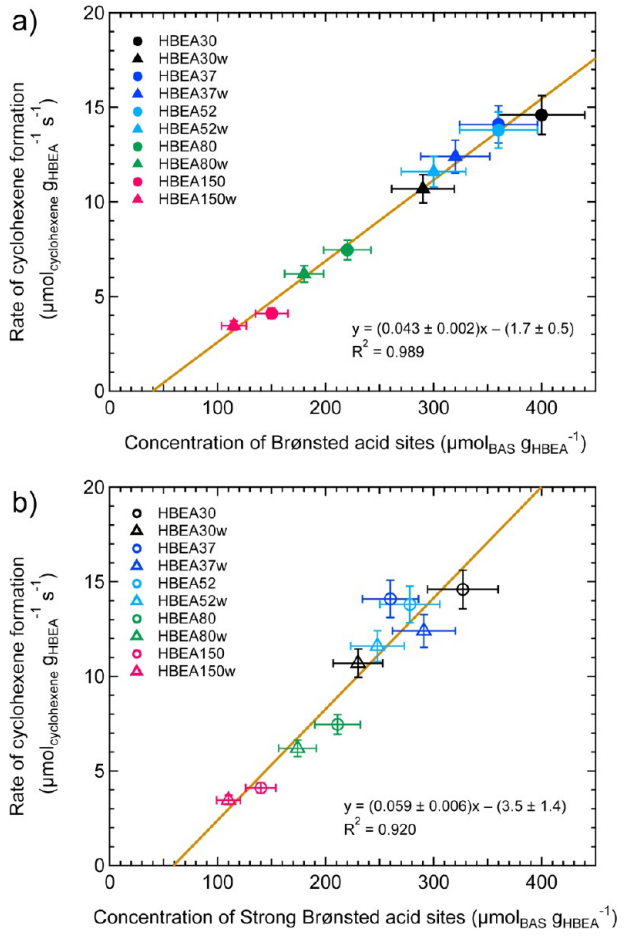

Figure 10. Rate of cyclohexene formation as a function of the concentration of (a) total (solid markers) and (b) strong (hollow markers) BAS determined by gas-phase pyridine adsorption. The color-coding for the 10 HBEA samples is reported in the legend. The correlations between measured rates and BAS concentrations as well as the respective slopes are also shown.

A correlation between the Al concentrations and the weight-normalized rates was not observed. Since the concentration of BAS was substantially lower (~50%) than the concentration of tetrahedrally coordinated Al (Table 1), we hypothesize that not all BAS are accessible to pyridine (blocked or being charge compensated by cations) or cyclohexanol. We conclude that the accessible fraction of strong and weak BAS have a similar activity because in the presence of water zeolite protons are present as hydrated H_3O^+ ions.[34] This, in turn, implies that the intrinsic acid site strength and catalytic performance is independent of acid strength of the parent dry zeolite.

The decrease in the BAS concentration in the presence of hot water is proposed to be retarded by decreasing the concentration of surface Si–OH groups as well as silanol-nests, which have been identified as sites initiating the framework decomposition.[35] Conceptually, zeolite framework stability, therefore, can be improved by minimizing the Si–OH concentration, either via synthesis or by postsynthesis chemistry (e.g., by converting two Si–OH groups to one Si–O–Si group).

CONCLUSION

The impact of the aqueous reaction medium on the activity of zeolites for acid-catalyzed reactions is studied on the example of cyclohexanol dehydration. The turnover frequency in water is proportional to the sum of the concentration of strong and weak Brønsted acid sites. This is attributed to the fact that the Brønsted acid sites of the solid formed hydrated hydronium ions. The location of Al T-sites in the zeolite did not affect the turnover frequency in aqueous medium, indicating that all hydrated hydronium ions have the same activity for alcohol dehydration. Exposure of the zeolite to hot water decreased the reaction rate. This was caused by framework hydrolysis of Si reducing the accessibility of tetrahedrally coordinated Al through charge compensation by cations as well as by pore or site blocking caused by dissolved and reprecipitated silica. The induced presence of oxidic species in the pores is shown by the reduction of the micropore volume. Only in the case of HBEA150 was the decrease in activity also associated with the conversion of a fraction of tetrahedral Al to octahedral coordination. Key to a new generation of active and stable catalysts is the reduction of the rate of hydrolysis of Si–O–Si bonds by lowering the concentration of the Si–OH groups either by design or by postsynthetic treatment. Detailed kinetic and synthetic experiments are underway to test the hypotheses and to enhance the stability of zeolites in water.

EXPERIMENTAL SECTION

Reagents. HBEA150 (Si/Al = 75) was obtained from Clariant in H-form. Cyclohexanol (Sigma-Aldrich, 99%), cyclohexene (Sigma-Aldrich, 99%, GC-grade), 1,3-dimethoxy-benzene (Sigma-Aldrich, 99%), dichloromethane (Sigma-Aldrich, HPLC grade), and sodium sulfate (Acros Organics, 99%, anhydrous) are used as-received without further purification.

Catalyst Preparation. HBEA zeolites are synthesized according to the procedure reported by M. Derewinski and F. Fajula.[36] The method is briefly reviewed on the example of HBEA30 (Si/Al = 15): 260.2 g of tetraethylammonium hydroxide (TEAOH) and 39.6 g of water are mixed in a polypropylene beaker. Then, 4.57 g of sodium aluminate is

DOI: 10.1021/jacs.5b06169
J. Am. Chem. Soc. 2015, 137, 10374–10382

added under vigorous stirring at room temperature (RT) until a clear solution was obtained. Next, 50.0 g of Zeosil 175mp (silica source, Rhone-Poulenc) is slowly added to the solution. The system is aged for 24 h at RT under vigorous stirring, and then, the aged gel is charged into an autoclave with a Teflon liner. The synthesis is performed at 150 °C for 40 h under stirring. The synthesis time (40 h) was identical for all synthesized zeolites. Choosing the appropriate concentration of sodium aluminate in the gel controls the Si/Al ratio in the zeolite. The white product (powder) is filtered and washed with deionized water until pH = 7.5. The material is dried overnight at 80 °C and subsequently calcined at 550 °C in the flow of dry air. The calcined material is ion-exchanged using a 0.1 M NH_4NO_3 solution at 80 °C for 2 h; the procedure is repeated 2 times. The zeolite in NH_3-form is treated for 8 h at 450 °C in 100 mL/min nitrogen flow to obtain the H-form (HBEA).

An example of typical sample preparation via hot liquid water treatment: 0.5 g of zeolite and 20 mL of deionized water are sealed in a Teflon lined autoclave and heated for 48 h at 160 °C. The autoclave is cooled using ice/water and the samples are centrifuged and dried in vacuum for 24 h prior to storing. Prior to catalyst characterization and catalytic testing, the HBEA samples are stored for 48 h in a desiccator over a saturated $Ca(NO_3)_2$ aqueous solution in order to achieve full hydration of the zeolite pores.

Catalyst characterization. The BET surface area and pore volume (Table 1), as well as pore size distributions, were determined by N_2 adsorption−desorption isotherms measured at 77.3 K using an ASAP2020 automatic BET-Sorptometer. The concentrations of Brønsted acid sites were determined using infrared spectroscopy (IR) with pyridine as probe molecule. The catalyst samples were activated in vacuum at 723 K for 1 h at a heating rate of 10 K min^{-1} from 423 to 723 K. Pyridine was adsorbed and equilibrated (1 mbar, 423 K) for 1 h. Subsequently, the sample was outgassed for 1 h in order to remove physisorbed molecules. The sample was then heated at a rate of 10 K min^{-1} from 423 to 723 K to allow partial pyridine desorption (removing molecules adsorbed on weak acid sites). The IR spectra were acquired after each step using a ThermoScientific Nicolet IR spectrometer. For calibration, a standard (Zeolite HZSM-5 with Si/Al = 45, acid site concentration = 360 μmol g^{-1}) was used.

Catalytic Testing. The catalytic testing was performed using the aqueous 0.33 M cyclohexanol dehydration at 160 °C as a test reaction. An example of a typical experiment using a zeolite catalyst: 58 mg of HBEA and 80 mL of 0.33 M cyclohexanol were sealed in a Hastelloy PARR reactor, pressurized to 50 bar using H_2 and stirred vigorously while heated to 160 °C. The reaction time was reported counting from the point when the set temperature was reached (∼12 min). Upon completion, the reactor was cooled using ice/water and the contents were extracted using dichloromethane. The organic phase was analyzed on an Agilent 7890A GC equipped with HP-5MS 25-m 0.25-μm i.d. column, coupled with Agilent 5975C MS. 1,3-Dimethoxybenzene was used as internal standard for compound quantification.

Al K-Edge XAFS. The Al K-edge XAFS measurements were performed at the Phoenix I, elliptical undulator beamline at the Swiss Light Source (SLS) at the Paul Scherrer Institute. Energy calibration was achieved by setting inflection point of an Al foil spectrum to 1559.6 eV. The double-crystal monochromator employed a set of $KTiOPO_4$ (011) crystals to provide an energy resolution of about 0.6 eV over a scan range for the Al K-edge from 1500 to 2150 eV. Two Ni-coated mirrors were set at an angle of 1.45° to provide cutoff of higher harmonics. An unfocused 1.0 × 1.0 mm beam having a flux of approximately 10^9 photons/s was used. The sample chamber pressure was maintained at approximately 2.5×10^{-4} mbar. Measurements were performed in fluorescence mode. I_0 was measured as total electron yield signal taken from a 0.5 μm thin polyester foil, which was coated with 50 nm of Ni. This I_0 detector was held in a miniaturized vacuum chamber (2.9×10^{-6} mbar), which was separated by a thin Kapton foil from the measurement chamber itself. The X-ray fluorescence was detected using a 4-element Vortex Si-drift diode detector. ATHENA[37] software was used during the background processing necessary to extract the $\chi(k)$ data from the background function. A Fourier filter cutoff distance, R_{bkg}, of 1.0 Å was used. The XAFS data were weighted by k^2, and truncated using a Hanning window with dk = 1.0 $Å^{-1}$ in the range of 1.5 < k < 8.0 $Å^{-1}$. Molecular dynamics (MD) EXAFS[38] was used to analyze the experimental EXAFS data for the series of HBEA samples. The analytical approach for determining the Al-distribution in HBEA from the EXAFS analysis has been described previously.[8] In short, on the basis of the BEA single crystal,[39] a DFT structure optimization of the zeolite T-sites (populating a single T-site of the unit cell with Al) was arranged into groups based on the similarities of the calculated EXAFS spectra. These groups were named Set A (T1, T2, T5, T6), Set B (T3, T4) and Set C (T7, T8, T9). In the next step, MD trajectory calculations were performed for a representative T-site from each set (T1, T3, T7 for A, B, C, respectively). Structures from these trajectories were used to calculate an EXAFS spectrum for each set. Finally, a linear combination of these MD-EXAFS calculated spectra along with the EXAFS spectrum of $Al(H_2O)_6^{3+}$, as a model of the octahedral Al sites, was used to fit the measured EXAFS spectra.[8]

X-ray Diffraction (XRD). XRD patterns were collected on a Rigaku Mini Flex II benchtop X-ray diffractometer using a Cu Kα radiation of 0.154056 nm (30 kV and 15 mA). Experiments were performed on a rotating powder sample holder in a 2θ range of 5° to 60° with a step size of 0.02°/s. All measurements were performed under ambient conditions.

^{27}Al MAS NMR. The Ultrahigh field ^{27}Al MAS NMR experiments were performed on a Varian-Agilent Inova 63 mm wide-bore 850 MHz NMR spectrometer. Experiments were performed using a commercial 3.2 mm pencil type MAS probe. In a typical experiment, about 15 mg of sample powder was loaded in the rotor and measured at ambient temperature. The HBEA samples were stored for 48 h in a desiccator over a saturated $Ca(NO_3)_2$ aqueous solution to reproducibly hydrate the zeolites. This procedure led to Al tetrahedra that have minimal distortions and that have the maximum ^{27}Al MAS NMR spectral resolution.[40] A single pulse sequence with a pulse length of 2.0 ms, corresponding to a pulse angle of 45°, was selected for acquiring each ^{27}Al MAS NMR spectrum with a recycle time of 1 s and total accumulation of 5000 scans. The spectra were acquired at a sample spinning rate of 20 kHz ± 2 Hz and were referenced to 1.5 M $Al(NO_3)_3$ in H_2O (0 ppm) using the center of the octahedral peak of solid γ-Al_2O_3 (at 13.8 ppm) as a secondary reference. For quantitative measurements, the weights of samples loaded into the MAS rotor were recorded and four spectra were acquired to check the stability of the spectrometer. The matching and tuning conditions of the RF circuit of the NMR probe were set using a network analyzer. All other experimental conditions were kept identical for all analyzed samples. In this way, the absolute peak areas normalized to the spectrometer standard were proportional to the Al in the sample. The spectra were analyzed using the MestreNova 8.1 software package.

^{29}Si MAS NMR. The single pulse (SP) and cross-polarization (CP) ^{29}Si MAS NMR experiments were performed using a Varian Inova 89 mm wide-bore 300 MHz NMR spectrometer and a 5 mm HXY MAS Chemagnetics style probe. The following parameters for the cross-polarization pulse sequence were used: the H90 was set to 3.5 μs, the contact time was 1 ms and the decoupling field of 62.5 kHz was applied for 10 ms during the acquisition time. The spinning speed was set to 5 kHz.

DFT Calculations. The NMR chemical shifts for the HBEA Al T-sites were calculated using the gauge invariant atomic orbital (GIAO) approach[41] in the NWChem software package.[42] The modeled clusters as well as further computational details are reported elsewhere.[8]

Helium Ion Microscopy (HIM). HIM images were obtained using 35 keV He ions with 0.1 pA beam current at normal incidence. Secondary electrons were detected using an Everhart-Thornley detector. Because the samples were completely insulating, a thin layer of carbon (<1 nm) was coated using a carbon sputter deposition system. The instrument resolution was 0.35 nm.

Abbreviations. DFT, density functional calculations; EXAFS, extended X-ray absorption fine structure spectroscopy; XANES, X-ray absorption near edge spectroscopy; MAS, magic angle spinning; NMR, nuclear magnetic resonance; MD, molecular dynamics; HDO, hydrodeoxygenation; XAFS, X-ray absorption spectroscopy; XSW,

DOI: 10.1021/jacs.5b06169
J. Am. Chem. Soc. 2015, 137, 10374−10382

X-ray standing wave; XRD, X-ray diffraction; TPD, temperature programed desorption.

■ ASSOCIATED CONTENT

Supporting Information

The Supporting Information is available free of charge on the ACS Publications website at DOI: 10.1021/jacs.5b06169.

XRD patterns, BET measurement data, NMR and EXAFS fit (PDF)

■ AUTHOR INFORMATION

Corresponding Author

*Johannes.Lercher@pnnl.gov

Notes

The authors declare no competing financial interest.

■ ACKNOWLEDGMENTS

Authors thank B. W. Arey (PNNL) for HIM measurements, T. Huthwelker for support during Al XAFS measurements at the Swiss Light Source (PSI, Switzerland), J. Z. Hu and S. D. Burton (PNNL) for support during NMR experiments. This work was supported by the U.S. Department of Energy (DOE), Office of Science, Office of Basic Energy Sciences, Division of Chemical Sciences, Geosciences & Biosciences. M.D. acknowledges support by the Materials Synthesis and Simulation Across Scales (MS^3 Initiative) conducted under Laboratory Directed Research & Development Program at PNNL. NMR experiments were performed at the Environmental Molecular Science Laboratory, a national scientific user facility sponsored by the DOE Office of Science, Office of Biological and Environmental Research, and Physical Science Laboratory both located at Pacific Northwest National Laboratory (PNNL).

■ REFERENCES

(1) Antal, M. J.; Carlsson, M.; Xu, X.; Anderson, D. G. M. *Ind. Eng. Chem. Res.* **1998**, *37*, 3820−3829.

(2) Zhao, C.; Lercher, J. A. *Angew. Chem., Int. Ed.* **2012**, *51*, 5935−5940.

(3) Pinkert, A.; Marsh, K. N.; Pang, S. S.; Staiger, M. P. *Chem. Rev.* **2009**, *109*, 6712−6728.

(4) Ravenelle, R. M.; Schüssler, F.; D'Amico, A.; Danilina, N.; van Bokhoven, J. A.; Lercher, J. A.; Jones, C. W.; Sievers, C. *J. Phys. Chem. C* **2010**, *114*, 19582−19595.

(5) Vjunov, A.; Fulton, J. L.; Camaioni, D. M.; Hu, J. Z.; Burton, S. D.; Arslan, I.; Lercher, J. A. *Chem. Mater.* **2015**, *27*, 3533−3545.

(6) Zapata, P. A.; Faria, J.; Ruiz, M. P.; Jentoft, R. E.; Resasco, D. E. *J. Am. Chem. Soc.* **2012**, *134*, 8570−8578.

(7) Zhao, C.; Kou, Y.; Lemonidou, A. A.; Li, X.; Lercher, J. A. *Chem. Commun.* **2010**, *46*, 412−414.

(8) Vjunov, A.; Fulton, J. L.; Huthwelker, T.; Pin, S.; Mei, D.; Schenter, G. K.; Govind, N.; Camaioni, D. M.; Hu, J. Z.; Lercher, J. A. *J. Am. Chem. Soc.* **2014**, *136*, 8296−8306.

(9) Brunauer, S.; Emmett, P. H.; Teller, E. *J. Am. Chem. Soc.* **1938**, *60*, 309−319.

(10) Barrer, R. M. *Zeolites and Clay Minerals as Sorbents and Molecular Sieves*; Academic Press, London, U.K., 1978.

(11) Rüscher, C. H.; Salman, N.; Buhl, J.−C.; Lutz, W. *Microporous Mesoporous Mater.* **2006**, *92*, 309−311.

(12) Zhdanov, S. P.; Khvoshchev, S. S.; Feoktistova, N. N. *Synthetic Zeolites*; Gordon & Breach Science Publishers: New York, NY, 1990; Vol. *1*.

(13) Wright, P. A.; Zhou, W.; Perez-Pariente, J.; Arranz, M. *J. Am. Chem. Soc.* **2005**, *127*, 494−495.

(14) van Bokhoven, J. A.; Sambe, H.; Ramaker, D. E.; Koningsberger, D. C. *J. Phys. Chem. B* **1999**, *103*, 7557−7564.

(15) Li, D.; Bancroft, G. M.; Fleet, M. E.; Feng, X. H.; Pan, Y. *Am. Mineral.* **1995**, *80*, 432−440.

(16) van Bokhoven, J. A.; van der Berden, A. M. J.; Koningsberger, D. C. *J. Am. Chem. Soc.* **2003**, *125*, 7435−7442.

(17) Maier, S. M.; Jentys, A.; Lercher, J. A. *J. Phys. Chem. C* **2011**, *115*, 8005−8011.

(18) van Bokhoven, J. A.; Koningsberger, D. C.; Kunkeler, P.; van Bekkum, H.; Kentgens, A. P. M. *J. Am. Chem. Soc.* **2000**, *122*, 12842−12847.

(19) Deng, F.; Yue, Y.; Ye, C. *J. Phys. Chem. B* **1998**, *102*, 5252−5256.

(20) Hunger, M.; Engelhardt, G.; Weitkamp, J. *Microporous Mater.* **1995**, *3*, 497.

(21) Perez-Pariente, J.; Sanz, J.; Fornes, V.; Corma, A. *J. Catal.* **1990**, *124*, 217−223.

(22) Schmidt−Rohr, K.; Spiess, H. W. *Multidimensional Solid-State NMR and Polymers*; Academic Press: London, 1994; ISBN 0-12-626630-1.

(23) Pinar, A. B.; Gomez-Hortguela, L.; McCusker, L. B.; Perez-Pariente, J. *Chem. Mater.* **2013**, *25*, 3654−3661.

(24) Gabova, V.; Dedecek, J.; Cejka, J. *Chem. Commun.* **2003**, 1196.

(25) Lippmaa, E.; Mägi, M.; Samoson, A.; Tarmak, M.; Engelhardt, G. *J. Am. Chem. Soc.* **1981**, *103*, 4992−4996.

(26) Čapek, L.; Dědeček, J.; Wichterlová, B. *J. Catal.* **2004**, *227*, 352−366.

(27) Fyfe, C. A.; Feng, Y.; Grondey, H.; Kokotailo, G. T.; Gies, G. *Chem. Rev.* **1991**, *91*, 1525.

(28) Hunger, M.; Kärger, J.; Pfeifer, H.; Caro, J.; Zibrowius, B.; Bülow, M.; Mostowicz, R. *J. Chem. Soc., Faraday Trans. 1* **1987**, *83*, 3459−3468.

(29) Zhuravlev, L. T. *Colloids Surf., A* **1993**, *74*, 71−90.

(30) Engelhardt, G.; Lohse, U.; Samoson, S.; Mägi, M.; Tarmak, M.; Lippmaa, E. *Zeolites* **1982**, *2*, 59−62.

(31) Lippmaa, E.; Samoson, A.; Brei, V. V.; Gorlov, Y. I. *Fiz. Chim.* **1981**, *259*, 403.

(32) Fyfe, C. A.; Gobbi, G. C.; Kennedy, G. J. *J. Phys. Chem.* **1985**, *89*, 277.

(33) Pines, A.; Gibby, M. G.; Waugh, J. S. *J. Chem. Phys.* **1973**, *59*, 569.

(34) Corma, A.; Lopez Agudo, A.; Fornes, V. *J. Chem. Soc., Chem. Commun.* **1983**, 942−944.

(35) Ravenelle, R. M.; Schüssler, F.; D'Amico, A.; Danilina, N.; van Bokhoven, J. A.; Lercher, J. A.; Jones, C. W.; Sievers, C. *J. Phys. Chem. C* **2010**, *114*, 19582−19595.

(36) Derewinski, M. A.; Fajula, F. *Appl. Catal., A* **1994**, *108*, 53−61.

(37) (a) Ravel, B.; Newville, M. *J. Synchrotron Radiat.* **2005**, *12*, 537. (b) Newville, M. *J. Synchrotron Radiat.* **2001**, *8*, 322.

(38) Palmer, B. J.; Pfund, D. M.; Fulton, J. L. *J. Phys. Chem.* **1996**, *100*, 13393−13398.

(39) Baerlocher, C.; McCusker, L. B., Database of Zeolite Structures, http://www.iza-structure.org/databases/ (accessed Jan 2015).

(40) Jiao, J.; Kanellopoulos, J.; Wang, W.; Ray, S. S.; Foerster, H.; Freude, D.; Hunger, M. *Phys. Chem. Chem. Phys.* **2005**, *7*, 3221−3226.

(41) Wolinski, K.; Hinton, J. F.; Pulay, P. *J. Am. Chem. Soc.* **1990**, *112*, 8251−8260.

(42) Valiev, M.; Bylaska, E. J.; Govind, N.; Kowalski, K.; Straatsma, T. P.; Van Dam, H. J. J.; Wang, W.; Nieplocha, J.; Apra, E.; Windus, T. L.; de Jong, W. A. *Comput. Phys. Commun.* **2010**, *181*, 1477.

DOI: 10.1021/jacs.5b06169
J. Am. Chem. Soc. 2015, 137, 10374−10382